1 **Tubulin Lattice in Cilia is in a Stressed Form Regulated by Microtubule Inner**

2 **Proteins**

3

4 Muneyoshi Ichikawa[1], Ahmad Abdelzaher Khalifa[1], Kaustuv Basu[2], Daniel Dai[1], Mohammad

5 Amin Faghfor Maghrebi[1], Javier Vargas[1], Khanh-Huy Bui[1,*]

6

7 [1]Department of Anatomy and Cell Biology, McGill University, Montréal, Québec, Canada, H3A

8 0C7

9 [2]Facility for Electron Microscopy Research, McGill University, Montréal, Québec, Canada, H3A

10 0C7

11 * **Corresponding author. E-mail: huy.bui@mcgill.ca**

12

13

14 **Short title:** Tubulin lattice is regulated by MIPs

15

16

17 **Abstract**

18 Cilia, the hair-like protrusions that beat at high frequencies to propel a cell or move fluid around

19 the cell, are composed of radially bundled doublet microtubules. The doublet microtubule is

20 composed of a 13-protofilament A-tubule, a partial 10-protofilament B-tubule and microtubule

21 inner proteins (MIPs) inside the tubulin lattice. In this study, we present the near-atomic

22 resolution map of the *Tetrahymena* doublet microtubules. The map demonstrates that the

23 network of microtubule inner proteins is weaving into the tubulin lattice, forming an inner sheath

24 of proteins. In addition, we also obtain the tubulin lattice structure with missing MIPs by Sarkosyl

25 treatment. In this structure, the tubulin lattice showed significant longitudinal compaction and

26 lateral angle changes between protofilaments. These results are evidence that the binding of

27 MIPs directly affects and stabilizes the tubulin lattice. It is also suggested that the doublet

28 microtubule is an intrinsically stressed filament and this stress could be exploited in the

29 regulation of ciliary waveforms.

30

1

Introduction

31

32 Microtubules are tubular structures composed of protofilaments (PFs) of α- and β-tubulin

33 heterodimers in eukaryotes and are responsible for structural support, tracks in intracellular

34 transport and organization of organelles. In the cilia, nine doublet microtubules (doublets) are

35 radially bundled to form an axonemal structure. The doublet is composed of a complete 13-PF A-

36 tubule and an incomplete 10-PF B-tubule (Fig. 1A). The doublet is the scaffold where ciliary

37 proteins, such as axonemal dyneins and radial spokes, are periodically docked (1). These proteins

38 are important to initiate and regulate the bending motion of the cilia. The doublet also serves as

39 the tracks for motor proteins kinesin-2 and dynein-2 carrying intraflagellar transport cargoes

40 towards the distal tip and back to the base of the cilia (2). Defects in ciliary proteins cause

41 abnormal motility and function, hence, leading to cilia-related diseases, such as primary cilia

42 dyskinesia and Bardet-Biedl syndrome (3).

43 In contrast to the singlet microtubules (singlets) that show cycles of growth and shrinkage called

44 dynamic instability (4), the doublets are highly stable both *in vivo* and after purification (5). In the

45 lumen of the doublet, microtubule inner proteins (MIPs) bind periodically with 48-nm repeating

46 unit to the tubulin lattice as shown by cryo-electron tomography (6-9). Subnanometer cryo-

47 electron microscopy (cryo-EM) structure of the doublet isolated from *Tetrahymena* cilia revealed

48 many new MIPs forming an inner sheath inside the doublet. This inner sheath is composed of

49 different classes of MIPs. In particular, there exists filamentous MIPs (fMIPs) composed of long

50 α-helices running between the inner ridges of the neighbouring PF pairs (5). It is reasonable to

51 speculate that these MIPs can exert its effects on inherent properties of the doublet such as

2

52   rigidity, damage resistance and stability similar to what microtubule-associated proteins affects

53   the properties of singlets (10).

54   Recently, Rib72a/b were characterized as components of MIPs inside the A-tubule of

55   *Tetrahymena* (11) while FAP45 and FAP52 were identified as MIPs in the B-tubule in

56   *Chlamydomonas* (10). The Rib72a/b knockout caused reduced *Tetrahymena* swimming speed.

57   The B-tubule of *Chlamydomonas* FAP45 and FAP52 double knockout mutant were more

58   vulnerable to depolymerization. These studies highlight the global effects of MIPs on motility and

59   stability of cilia. The resolution of the doublet structures presented in these studies, however,

60   was insufficient to uncover how these proteins affect the tubulin lattice. In this study, we

61   obtained near-atomic resolution maps of the doublet and the fractionated A-tubule from

62   *Tetrahymena* cilia to understand the influence of MIPs to the tubulin lattice.

63   **Results**

64   **A weaving network of MIPs inside the tubulin lattice**

65   To gain insights into the molecular architecture of the doublet, we obtained a 4.3 Å resolution

66   cryo-EM map of the 48-nm repeating unit of the purified doublet from Tetrahymena cilia (Fig.

67   S1). This map shows the details of MIPs inside the doublet (Fig. 1 B to E; Fig. S1; and Movie S1;

68   see also the supplementary text). The MIP densities are named based on locations as in (5). At

69   this resolution, it becomes clear that each designated MIP can contain multiple polypeptides.

70   Instead of simply binding on the inside surface of the doublet, MIPs consist of many branches,

71   mainly α-helical, which weave into the tubulin lattice of the doublet (Fig. 1C). In particular, some

72   long α-helical MIP branches poke through the A-tubule into the lumen of the B-tubule (Fig. 1 D

73   and Fig. S1, H to M). Remarkably, we also observed MIP branches lace through the A- and B-

74   tubule to the outside, a phenomenon that has never been observed with other microtubule

75   associated proteins. For instance, a part of MIP2 goes through the lateral gap among PF A10, A11

76   and B1 to the outside of the doublet (Fig. 1D and Movie S1). The branch of fMIP-A6A7 also weaves

77   through the tubulin lattice to be in contact with outside densities (Fig. 1E), which correspond to

78   region of outer dynein arm. Outside the B-tubule, there are a lot of densities in the groove

79   between PF pairs from B3 to B9 (Fig. 1, A and B; Fig. S1H; and Movie S1). These densities contact

80   the fMIPs in the B-tubule through protrusion in the tubulin lattice.

81   This weaving network of MIPs is more complex in the A-tubule consisting of majorly globular

82   MIPs and some fMIPs, while the B-tubule mainly has fMIPs. As expected from the presence of

83   the extensive weaving network of MIPs inside, the A-tubule was more stable compared with the

84   B-tubule. After sonication, singlet A-tubules with their B-tubules physically broken were observed

85   (Fig. S1, A and C). Treatment of the doublet with 0.2% Sarkosyl also disintegrated the B-tubule

86   leaving the A-tubule portion as in (12) (Fig. S1, A, B, and D). This shows the importance of the

87   MIPs in stabilizing the tubulin lattice. For a singlet, mechanical stress from repeated cycles of

88   bending and release was shown to induce local damage in the tubulin lattice (13). This effect will

89   be more severe in motile cilia, which beat at high frequency for long periods of motility.

90   Using EM images of sonicated and Sarkosyl treated fraction, we obtained two types of A-tubule

91   structures (sonicated and Sarkosyl A-tubules) at 4.4 and 4.9 Å resolution (Fig. 2 A and B, and Fig.

92   S1E). While the sonicated A-tubule structure retained all the MIPs inside the tubulin lattice, the

93   Sarkosyl A-tubule structure was missing some MIP densities (Fig. 2C). Multiple densities at MIP4

94   area were affected by Sarkosyl treatment and a part of MIP6 was missing (Fig. 2 D and E and Fig.

95   S2 A and B). Other MIP densities inside the Sarkosyl A-tubule were less-well resolved, suggesting

96   they were partially removed or became flexible (Fig. 2C).

97   **MIPs regulate the compaction state of the tubulin lattice**

98   In the near-atomic resolution maps, we were able to observe the conformation of each tubulin

99   dimer in the 48-nm unit (Fig. S1G). Recently published structures of singlets show changes in the

100   longitudinal tubulin dimer distance depend on the nucleotide states of the β-tubulin (14-18).

101   Stable microtubules in GTP state have elongated dimer distance while the less stable GDP-state

102   singlet microtubules have a compacted dimer distance (19).

103   In the doublet, densities of GTP and GDP are observed in the α- and β-tubulin respectively (Fig.

104   S3). Therefore, the tubulin lattice in the doublet is in GDP state. The average dimer distance of

105   the doublet was 83.1 Å (Fig. 3 A and B, and Table S1), which is comparable to the elongated GTP-

106   type distance in singlets (15). When MIPs are missing, the lattice of Sarkosyl A-tubule showed

107   significant compaction and the average dimer distances became 81.1 Å (Fig. 3 B to F; Fig. S3;

108   Table S1; and Movie S2), which is considered as a GDP-type compacted lattice (15). Since the

109   sonicated A-tubule did not show compaction (Fig. S4I and Table S1), loss of MIPs, instead of the

110   removal of the B-tubule caused compaction of the lattice.

111   There was also a variation of tubulin dimer distances among PFs and even among the same PF

112   both in our doublet and A-tubule maps (Fig. 3B and Fig. S4, see also the supplementary text). This

113   leads to an extremely heterogenous tubulin lattice compared with the singlet (Fig. S4B). Even

114   within the same PF, tubulin dimer distances varied within the 48-nm unit. On the other hand,

115   since we consistently observe this heterogeneity of tubulin lattice distance in our maps averaged

116   from thousands of cryo-EM particles, the weaving network of MIPs is able to tightly and precisely

117 regulate this heterogeneity within its repeating unit. The dimer distances in a few PFs (PFs-A1,

118 A11-13) showed bimodal distributions with ~2 Å differences with an oscillatory pattern (Fig. 3B

119 and Fig. S4C, D). The existence of the bimodal distribution in the Sarkosyl A-tubule suggests that

120 remaining MIPs determines the tubulin dimer distances. Indeed, the branches from fMIPs-

121 A11A12 and A12A13 were forming coiled-coils and poking into the tubulin lattice between PFs-

122 A12 and A13 every 16-nm (Fig. S1L, M), which coincides with the repeating unit of tubulin dimer

123 distance change of PFs-A12 and A13 (Fig. S4C).

124 The lattice length difference within and between PFs creates tension inside the filament; hence,

125 the doublet is an inherently stressed filament. Previous study showed that doublets purified from

126 sea urchin sperm flagella form helical structures depending on pH or calcium ion concentration

127 (20). This means that the degree of inherent tension inside the doublet can be changed by

128 external cues. There are a few MIP candidates with calcium binding domain, such as Rib72a (11)

129 and FAP85 (21). Thus, MIPs can exploit the tubulin conformational change as a tool to modify the

130 rigidity of the doublet and, thus, ciliary bending (Fig. 3G).

131 **MIPs affect the curvature of the doublet**

132 In addition to changes in lattice compaction, we also observed changes in angles between PFs

133 (Fig. 4A and Fig. S5A). Unlike 13-PF singlet which is a near perfect circle, the A-tubule of doublet

134 showed squashed shape as in (5) with a variety of angles between PFs (Fig. 4A). Compared to the

135 doublet, the PF angles from the Sarkosyl A-tubule showed significant changes at PF pairs, such as

136 A1/A2 and A12/A13 (Fig. 4A and Table S3) where MIPs were missing (Fig. 2C and Fig. S2). The

137 Sarkosyl A-tubule's PF pair-A12/A13, where several MIP4 densities were lost, showed the largest

138 change of angle even when compared to the sonicated A-tubule (Fig. 4A and Fig. S5B). The lateral

6

139   curvature between PF pairs-A12/A13 of the doublet was equivalent to the curvature of the 22-

140   PF singlet, which is highly energetically unfavorable considering *in vitro* reconstituted singlets

141   generally take the 11-16 PF structure (22). With the loss of MIP4, the curvature shifted towards

142   a more relaxed conformation comparable to the 18-PF singlet (Fig. 4 B and C). Therefore, some

143   MIPs work as a molecular binder to keep the tubulin lattice at a higher degree of curvature while

144   other MIPs serve as a molecular wedge that open neighboring PFs to flatten the degree of

145   curvature (Fig. 4D).

146   The influence of MIPs on the local curvatures can be additive since the curvature of PF pair-

147   A12/A13 after the loss of MIP4 densities is still in the energetically unfavourable range (Fig. 4A).

148   PF pair-A9/A10 also showed a slight change in the angle without any MIPs missing (Fig. 4A). This

149   is the location of the seam (5) (Fig. S1G) where the lateral interaction between PFs is the weakest

150   (15). Thus, this slight angle change can be a result of the tubulin lattice accommodating the local

151   angle changes. The global effect of local PF angle changes can be seen as a slight shift of the

152   tubulin lattice in the map (Fig. 2 A to C).

153   **Discussion**

154   Our results are the direct evidence that MIPs directly influence the tubulin lattice architecture,

155   i.e. curvature and tubulin dimer distance from the inside. The MIPs work in a coordinated fashion

156   to keep the doublet in a stable and distorted circle that likely facilitates the specific and proper

157   formation of the B-tubule (5). The network of MIPs prevents the loss of tubulins and spontaneous

158   breakage in the middle of the tubulin lattice by weaving into the tubulin lattice as an integrated

159   layer (Fig. 5). Recently, *in vitro* reconstruction of doublet was achieved from subtilisin-treated

160   tubulins with more flexibility of the B-tubule (23). This suggests that MIPs can limit the C-terminal

161   conformation *in vivo* for the initial binding of the B-tubule and also stabilize the tubulin binding

162   to the outside surface of the A-tubule. Therefore, the MIPs might play an important role in

163   facilitating the assembly of the doublet.

164   Recent studies demonstrate that the elongation and compaction of the tubulin lattice of singlets

165   plays an important role in the dynamic instability of microtubule (14-18). Binding of microtubule

166   associated proteins can have a direct effect on the lattice compaction and, hence, microtubule

167   dynamics (18). Our results suggest that in the doublet, the MIPs function as a molecular jack to

168   regulate the dimer distance of the tubulin lattice in an elongated state (Fig. 3G). This points to a

169   common mechanism where the lattice maintenance is used to regulate to microtubule stability

170   and as the result, regulate further properties such as waveforms in the cilia.

171   Herein, we propose a lattice centric model for the cilia in which the doublet tubulin lattice serves

172   as a platform to integrate the signals of binding of the MIPs and outer proteins. Binding of the

173   MIPs leads to the local and global lattice rearrangement which affects the affinity of the outer

174   proteins like axonemal dyneins and radial spokes. This allows the assembly of the complex

175   axoneme in an orderly fashion (1), and thereby proper ciliary beating. The unique dimer distances

176   among different PFs and the inside-to-outside connection can also influence the intraflagellar

177   transport motors like kinesin-2 and dynein-2 to have different affinities and consequently use B-

178   and A-tubule separately for transport (2).

8

190 **REFERENCES AND NOTES**

191 1. Bui KH, Yagi T, Yamamoto R, Kamiya R, & Ishikawa T (2012) Polarity and asymmetry in
192 the arrangement of dynein and related structures in the Chlamydomonas axoneme. *The*
193 *Journal of cell biology* 198(5):913-925.

194 2. Stepanek L & Pigino G (2016) Microtubule doublets are double-track railways for
195 intraflagellar transport trains. *Science* 352(6286):721-724.

196 3. Fliegauf M, Benzing T, & Omran H (2007) When cilia go bad: cilia defects and
197 ciliopathies. *Nature reviews. Molecular cell biology* 8(11):880-893.

198 4. Akhmanova A & Steinmetz MO (2008) Tracking the ends: a dynamic protein network
199 controls the fate of microtubule tips. *Nature reviews. Molecular cell biology* 9(4):309-
200 322.

201 5. Ichikawa M*, et al.* (2017) Subnanometre-resolution structure of the doublet microtubule
202 reveals new classes of microtubule-associated proteins. *Nature communications*
203 8:15035.

204 6. Nicastro D*, et al.* (2006) The molecular architecture of axonemes revealed by
205 cryoelectron tomography. *Science* 313(5789):944-948.

206 7. Nicastro D*, et al.* (2011) Cryo-electron tomography reveals conserved features of
207 doublet microtubules in flagella. *Proceedings of the National Academy of Sciences of the*
208 *United States of America* 108(42):E845-853.

209 8. Sui H & Downing KH (2006) Molecular architecture of axonemal microtubule doublets
210 revealed by cryo-electron tomography. *Nature* 442(7101):475-478.

211 9. Pigino G*, et al.* (2012) Comparative structural analysis of eukaryotic flagella and cilia
212 from Chlamydomonas, Tetrahymena, and sea urchins. *Journal of structural biology*
213 178(2):199-206.

214 10. Mikito Owa TU, Haruaki Yanagisawa, Takashi Yamano, Hiro Iguchi, Hideya Fukuzawa,
215 Ken-ichi Wakabayashi, Toshio Ando, Masahide Kikkawa (2018) Inner lumen proteins
216 stabilize doublet microtubules in cilia/flagella. *BioRvix*.

217 11. Stoddard D*, et al.* (2018) Tetrahymena RIB72A and RIB72B are microtubule inner
218 proteins in the ciliary doublet microtubules. *Molecular biology of the cell* 29(21):2566-
219 2577.

220 12. Linck RW (1976) Flagellar doublet microtubules: fractionation of minor components and
221 alpha-tubulin from specific regions of the A-tubule. *Journal of cell science* 20(2):405-439.

222 13. Schaedel L*, et al.* (2015) Microtubules self-repair in response to mechanical stress. *Nat*
223 *Mater* 14(11):1156-1163.

224 14. Alushin GM*, et al.* (2014) High-resolution microtubule structures reveal the structural
225 transitions in alphabeta-tubulin upon GTP hydrolysis. *Cell* 157(5):1117-1129.

226 15. Zhang R, Alushin GM, Brown A, & Nogales E (2015) Mechanistic Origin of Microtubule
227 Dynamic Instability and Its Modulation by EB Proteins. *Cell* 162(4):849-859.

228 16. Manka SW & Moores CA (2018) The role of tubulin-tubulin lattice contacts in the
229 mechanism of microtubule dynamic instability. *Nature structural & molecular biology*
230 25(7):607-615.

231 17. Zhang R, LaFrance B, & Nogales E (2018) Separating the effects of nucleotide and EB
232   binding on microtubule structure. *Proceedings of the National Academy of Sciences of*
233   *the United States of America* 115(27):E6191-E6200.
234 18. Zhang R, Roostalu J, Surrey T, & Nogales E (2017) Structural insight into TPX2-stimulated
235   microtubule assembly. *Elife* 6.
236 19. Manka SW & Moores CA (2018) Microtubule structure by cryo-EM: snapshots of
237   dynamic instability. *Essays Biochem* 62(6):737-751.
238 20. Miki-Noumura T & Kamiya R (1979) Conformational change in the outer doublet
239   microtubules from sea urchin sperm flagella. *The Journal of cell biology* 81(2):355-360.
240 21. Kirima J & Oiwa K (2018) Flagellar-associated Protein FAP85 Is a Microtubule Inner
241   Protein That Stabilizes Microtubules. *Cell Struct Funct* 43(1):1-14.
242 22. Sui H & Downing KH (2010) Structural basis of interprotofilament interaction and lateral
243   deformation of microtubules. *Structure* 18(8):1022-1031.
244 23. Schmidt-Cernohorska M*, et al.* (2019) Flagellar microtubule doublet assembly in vitro
245   reveals a regulatory role of tubulin C-terminal tails. *Science* 363(6424):285-288.
246
247
248
249
250

Materials and Methods

Sample preparation

Tetrahymena doublet microtubule fragments were prepared as in Ichikawa *et al*., (5) (fig. S1, A and B). In brief, *Tetrahymena* cells (SB255 strain) were cultured in 1L of SPP media [1% proteose peptone No.3, 0.2% glucose, 0.1% yeast extract, 0.003% ethylenediaminetetraacetic acid ferric sodium salt (Fe-EDTA)]. Cilia were isolated by dibucaine method (24) and resuspended in cilia final buffer [CFB; 50 mM 4-(2-hydroxyethyl)-1-piperazineethanesulfonic acid (HEPES), pH 7.4, 3 mM $MgSO_4$, 0.1 mM ethylene glycol tetraacetic acid (EGTA), 0.5% Trehalose, 1 mM dithiothreitol (DTT)] containing 1 mM phenylmethylsulfonyl fluoride (PMSF). Cilia were de-membraned by adding final 1.5% NP-40, split by adding final 0.4 mM ATP, and incubated in CFB containing 0.6 M NaCl for 30 min on ice twice to remove dyneins. *Tetrahymena* doublets dialyzed against low salt buffer [5 mM HEPES, pH 7.4, 1 mM DTT, 0.5 mM ethylenediaminetetraacetic acid (EDTA)] to deplete radial spokes were fragmented by sonication and resuspended in CFB containing 0.6 M NaCl to avoid aggregation of doublet fragments.

For the Sarkosyl A-tubule, the doublets after twice 0.6 M NaCl treatment and dialysis were incubated with CFB containing 0.2% Sarkosyl to remove the B-tubule for 10 min on ice. Sonication was not performed on this sample prior to electron microscopy.

Electron Microscopy

3.5 μl of sample of fragmented doublets (~4 mg/ml) or the Sarkosyl A-tubule (~500 μg/ml) was applied to a glow-discharged holey carbon grid (Quantifoil R2/2), blotted and plunged into liquid ethane using Vitrobot Mark IV (Thermo Fisher Scientific) at 25℃ and 100% humidity with a blot force of 3 or 4 and a blot time of 5 sec. Movies of seven frames were obtained on a Titan Krios (Thermo Fisher Scientific) equipped with Falcon II camera at 59,000 nominal magnification. The calibrated pixel size was 1.375 Å/pixel. Both datasets for the doublet and Sarkosyl A-tubule were obtained with a total dose of ~30-45 electrons/$Å^2$. The defocus range was set to between -1.2 and -3.8 μm.

Image Processing

The movies were motion corrected and dose-weighted using MotionCor2 (25) implemented in Relion3 (26) and the contrast transfer function parameters were estimated using Gctf (27). After

280 discarding micrographs with apparent drift and ice contamination, bad contrast transfer function

281 estimation, 7,838 micrographs for doublet and 5,179 micrographs for Sarkosyl treated A-tubule

282 were used, respectively. The filament (doublet and A-tubule) were picked using e2helixboxer

283 (28). Since the preparation of doublet yields both doublets and A-tubules (fig. S1A), we also

284 picked the A-tubule from the micrographs for the doublet.

285 Reconstruction of the 48-nm of the doublet and A-tubule was done according to (5). In brief,

286 60,386 and 36,375 particles for doublet and A-tubule yielded maps of 4.7 and 4.8 Å resolution.

287 40,850 particles for Sarkosyl A-tubule yield 5.2 Å resolution map. After iterative per-particles-

288 defocus refinement and Bayesian polishing in Relion 3, the resolutions of the doublet, sonicated

289 A-tubule and Sarkosyl A-tubule improve to 4.3, 4.4 and 4.9 Å, respectively. The doublet and

290 sonicated A-tubule maps were sharpened using Relion-3 with a B-factor of -190 and -179 Å^2,

291 respectively.

292 Since the Sarkosyl A-tubule map exhibited a slightly preferred orientation and resolution

293 heterogeneity in the structure, we performed a local restoration and local sharpening (Javier *et*

294 *al*., manuscript in preparation) to reduce artifact from preferred orientation and resolution

295 heterogeneity. To ensure the local restoration and local sharpening does not alter the maps, we

296 also performed the local restoration and local sharpening on the doublet and A-tubule. There

297 was no artifact observed compared with global sharpening.

298 **Difference Map**

299 To reliably identify the densities missing in the Sarkosyl A-tubule, the unsharpened maps of the

300 sonicated and Sarkosyl A-tubule were filtered to 6 Å before performing difference mapping in

301 Chimera. After the subtraction, the regions of difference were mapped onto the Sarkosyl A-

302 tubule map as shown in Fig. 1H.

303 **Modelling**

304 Models of the α- and β-tubulins from *Tetrahymena* (Uniprot IDs: P41351, P41352) were

305 constructed by homology modelling in Modeller v9.19 (29) using *Sus scrofa* tubulin structure

306 (PDB: 3JAR) as a template. The homology models of the α- and β-tubulin dimers were refined in

307 the doublet map using Phenix (30). With our asymmetric structure of 48-nm periodicity, we were

13

308   able to model, dock and refine all six individual tubulin dimers within the 48-nm structure in each

309   individual PF of the doublet, sonicated and Sarkosyl A-tubules.

310   **Intra and inter-dimer distance measurement**

311   The α- and β-tubulin can be clearly distinguished in the maps. We docked in the atomic models

312   of the α- and β-tubulins in the map separately. The intra-dimer distance was measured as the

313   distance between the N9 of GTP in the α-tubulin and GDP in the β-tubulin of the same tubulin

314   dimer in Chimera. The inter-dimer distance was measured between N9 of GDP of the α-tubulin

315   and GDP in the β-tubulin in the next tubulin dimer. The dimer distance was calculated as a sum

316   of the intra- and inter-dimer distances.

317   **PF pair rotation angle (lateral curvature) measurement**

318   The lateral curvature can be represented by the lateral rotation angle between each PF pair. The

319   rotation angles and Z-shift between PF pairs were measured using the 'measure' command from

320   UCSF Chimera (31) according to Ichikawa *et al.*, (5).

321   **Visualization**

322   The maps and models were segmented, coloured and visualized using Chimera (31) and ChimeraX

323   (32).

324   **Data availability**

325   The dataset analysed and raw data of the measurements are available from the corresponding

326   author upon fair request.

327   # Supplementary Text

328   **MIPs**

329   MIP densities have been historically named as MIP1-7 and fMIPs, it is clear that each MIP

330   structure can contain multiple polypeptides. For example, after Sarkosyl treatment, the tip region

331   of MIP1 was missing but the base region of MIP1 was retained (Fig. 2, A to C). MIP4 densities

332   were widely affected by Sarkosyl treatment and part of MIP4b, c and d were lost (naming based

333   on (5)) (Fig. 2 and S2). However, fMIP-A11A12 remained intact. This means that the globular

334   densities and filamentous densities are composed of different polypeptides. Similarly, MIP6c

335   region (Fig. 2) is formed by distinct polypeptide from the rest of MIP6 (MP6a, b and d) consistent

336   with (11). In our map, MIP6c appears clearly as a two-domain structure, and thus named as

337 MIP6c-1 and c-2 here. From the appearance of the MIP network, it is reasonable to estimate at

338 least 30-40 polypeptides are present inside the doublet. This view is supported by the mass

339 spectrometry of the high-salt treated axoneme of *Chlamydomonas*, showing hundreds of

340 proteins, including proteins from the central pairs (33).

341 Both sonicated and Sarkosyl A-tubule maps lack B-tubule as well as MIPs binding outside the A-

342 tubule (MIP3, MIP5 and MIP7). This suggests that most of the MIPs in the B-tubule are connected.

343 They act as binders fixing the B-tubule onto the A-tubule and get removed together with the B-

344 tubule.

345 **Outside densities**

346 In our map, we can see the molecular ruler (34) binding to the outside furrow of PF pair-A2/A3.

347 Even at this resolution, we did not observe any connection between the MIPs and the molecular

348 ruler. Since the molecular ruler repeats with 96-nm periodicity (34), a 96-nm repeating unit

349 structure might be needed to clearly describe if there is interaction or not.

350 In this study, we observed a few outside densities in our doublet structure even after the high-

351 salt wash. First, there are filament-like densities in the outside wedge of PF pair-A6/A7 (shown in

352 blue in Fig. 1 A to C; Fig. S1K; and Movie S1). These densities seem to be in contact with densities

353 from the inside fMIP-A6A7 (red arrowheads in Fig. 1E and Fig. S1K). It is likely that the outside

354 filament-A6A7 are a part of the outer dynein arm complex since it is located close to the binding

355 site and these densities appear to have 24-nm periodicity, the periodicity of outer dynein arms.

356 These inside-to-outside interactions through the tubulin lattice could coordinate the protein

357 binding to outside and inside of doublet microtubule with different repeating units.

358 Outside the B-tubule, between PF pairs B3-B9, there exists outside densities (Fig. 1 A and B; Fig.

359 S1H; and Movie S1). These densities contact the fMIPs in the B-tubule through protrusion in the

360 tubulin lattice. Unlike the molecular ruler and outside densities of PFs A6/A7 seem filamentous,

361 these densities do not appear filamentous. However, this is a region with lower resolution than

362 the rest of the doublet, therefore, it is not conclusive.

363 **Branches of MIPs and connections to outside surface**

364 Apart from the connections mentioned in the previous section, there are many more inside-to-

365 outside connections. The branches of fMIP-A6A7 protrude into the tubulin lattice (Fig. 1E). These

15

366   protrusions are likely to contact the outer dynein arm ruler between PF-A7/A8 binding outside *in*

367   *vivo* ((35), fig. S1F).

368   The previously identified insertions (5) from MIP2 from inside of the A-tubule to the lumen of the

369   B-tubule is now clearly observed as two long α-helices per 48-nm repeat (Fig. 1 B to D). These

370   helices connect with densities from MIP7 in between PF pair B1 and A11. In addition, there is a

371   loop-like density from MIP2 protrude outside the A-tubule and into the gap between PFs-A10

372   and B1 (Fig. S1I). This density is likely to be exposed to the outside of the doublet. Though MIP2

373   and MIP7 are connected by the branches, they are likely to be composed of different

374   polypeptides since we see branches from MIP2 are present in A-tubule structures but MIP7 are

375   not (Fig. 2 A and B). These outside densities or insertions could act like the mean to recruit other

376   proteins like outside assembly scaffold, molecular motors, tubulin modifying enzymes.

377   **Tubulin conformation**

378   For the compaction of the lattice, it can also be observed as shifts of remaining MIPs as well as

379   tubulins in the maps (Fig. S2, and S4). The change in dimer distance is not accomplished through

380   perpendicular movement to the longitudinal axis of the doublet. The tubulins are tilted in a zig-

381   zag fashion and are compressed in an axis oblique of the longitudinal axis of the doublet (Fig. 3 E

382   and F).

383   It is also noteworthy that we can measure individual tubulins in the 48-nm repeats of the doublet

384   due to its asymmetric nature while the dimer distance measured from singlets are based on

385   tubulin structure averaged longitudinally and laterally. In our doublet map, lattice lengths were

386   not uniform, and every PF has a unique average dimer distance (Fig 3B; Fig. S4; and Table S1),

387   which are extremely heterogeneous compared with the singlet (Fig. S4B). Even within the same

388   PF, tubulin dimer distances varied within the 48-nm unit.

389   *Tetrahymena* tubulin lattice showed an inter-dimer distance of 41.7 ± 0.094 Å for doublet and

390   40.8 ± 0.159 Å for Sarkosyl A-tubule and intra-dimer distance of 41.3 ± 0.519 Å for doublet and

391   40.3 ± 0.486 Å for Sarkosyl A-tubule (Table S1). The deviation of intra-dimer distance was larger

392   than that of inter-dimer distance. This agrees with other studies on microtubule structure where

393   the inter-dimer distance is more flexible to change from nucleotide states (16). On the other

394   hand, the compressed Sarkosyl A-tubule has shorter averaged intra-dimer distances and hence

16

395   shorter dimer distances compared with singlet microtubule. The shortest dimer distance

396   observed in the Sarkosyl A-tubule is 79.9 Å, which is shorter than any reported tubulin dimer

397   distance (19). This could be either doublet microtubule specific feature or intrinsic feature of

398   *Tetrahymena* tubulin. Structural analysis using doublets from other species in future studies

399   would reveal this point.

400   This bimodal pattern of alternating long and shot dimer distances results in a significantly larger

401   interaction interface at the short distance pairs compared with the long-distance pairs (Fig. S4K).

402   In the case of Sarkosyl A-tubule, the compression of the tubulin lattice increases this interface

403   significantly. In addition, while there is a huge variation in the dimer distance among PFs, in most

404   cases, the differences in the dimer distance between neighbouring PFs are quite small allowing

405   the tubulin lattice to accommodate accumulative large changes (Fig. S4B).

406   The lattice length of the B-tubule is slightly shorter than the A-tubule as in (Fig. S4, I and J).

407   Previously, the doublet from sea urchin sperm was found to form spring-like structure and this

408   was proposed to be due to shorter B-tubule lattice than A-tubule (20) consistent with our

409   observation. The average dimer distances in the group of PFs A9-A2 and B1-B10 are 82.6 and 82.4

410   Å, corresponding to 0.5 and 0.9% shorter than the group of PFs A3-A8 (83.1 Å).

Author Contributions

412   KHB and MI designed the experiments and MI performed cell culture, purification, vitrification of

413   cryo grids. MI and KB performed cryo-EM data acquisition. MI, AK and KHB performed EM data

414   processing with helps from DD and MAFM. AK performed modelling of tubulin structure. MI and

415   KHB interpreted the data and wrote the manuscript.

416

Supplementary movie legends

Movie S1. Complex network of MIPs inside the doublet tubulin lattice.
MIPs inside the doublet tubulin lattice were connected and forming a complex network. Some branches were reaching even outside surface.
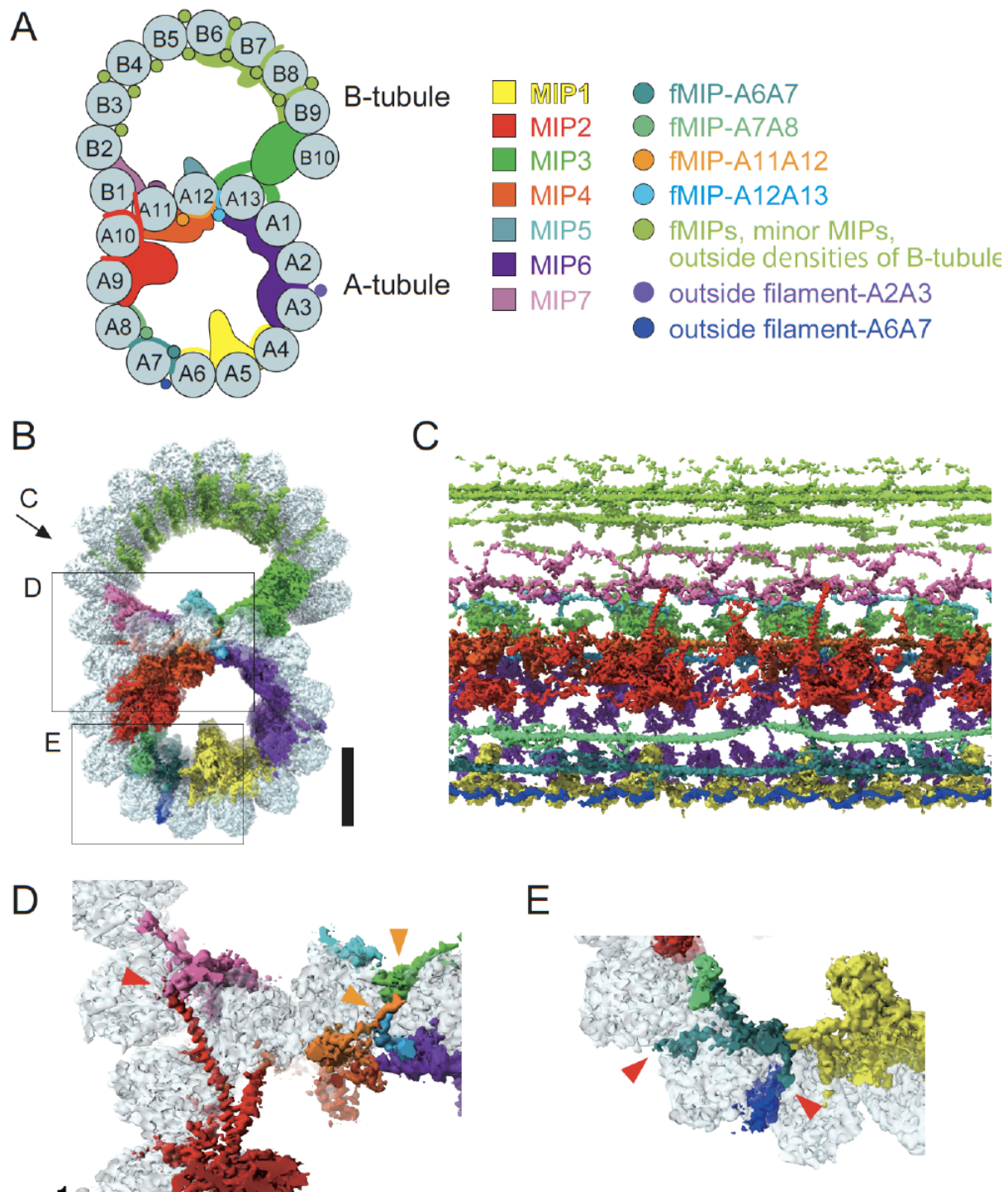
Movie S2. Comparison of tubulin lattice models from doublet and Sarkosyl A-tubule.
Tubulin models based on PF-A12 were morphed. After the Sarkosyl treatment, tubulin lattice showed a significant longitudinal compaction.

Supplementary References and Notes

1.   Bui KH, Yagi T, Yamamoto R, Kamiya R, & Ishikawa T (2012) Polarity and asymmetry in the arrangement of dynein and related structures in the Chlamydomonas axoneme. *The Journal of cell biology* 198(5):913-925.

2.   Stepanek L & Pigino G (2016) Microtubule doublets are double-track railways for intraflagellar transport trains. *Science* 352(6286):721-724.

3.   Fliegauf M, Benzing T, & Omran H (2007) When cilia go bad: cilia defects and ciliopathies. *Nature reviews. Molecular cell biology* 8(11):880-893.

4.   Akhmanova A & Steinmetz MO (2008) Tracking the ends: a dynamic protein network controls the fate of microtubule tips. *Nature reviews. Molecular cell biology* 9(4):309-322.

5.   Ichikawa M*, et al.* (2017) Subnanometre-resolution structure of the doublet microtubule reveals new classes of microtubule-associated proteins. *Nature communications* 8:15035.

6.   Nicastro D*, et al.* (2006) The molecular architecture of axonemes revealed by cryoelectron tomography. *Science* 313(5789):944-948.

7.   Nicastro D*, et al.* (2011) Cryo-electron tomography reveals conserved features of doublet microtubules in flagella. *Proceedings of the National Academy of Sciences of the United States of America* 108(42):E845-853.

8.   Sui H & Downing KH (2006) Molecular architecture of axonemal microtubule doublets revealed by cryo-electron tomography. *Nature* 442(7101):475-478.

9.   Pigino G*, et al.* (2012) Comparative structural analysis of eukaryotic flagella and cilia from Chlamydomonas, Tetrahymena, and sea urchins. *Journal of structural biology* 178(2):199-206.

10.   Mikito Owa TU, Haruaki Yanagisawa, Takashi Yamano, Hiro Iguchi, Hideya Fukuzawa, Ken-ichi Wakabayashi, Toshio Ando, Masahide Kikkawa (2018) Inner lumen proteins stabilize doublet microtubules in cilia/flagella. *BioRvix*.

11.   Stoddard D*, et al.* (2018) Tetrahymena RIB72A and RIB72B are microtubule inner proteins in the ciliary doublet microtubules. *Molecular biology of the cell* 29(21):2566-2577.

12.   Linck RW (1976) Flagellar doublet microtubules: fractionation of minor components and alpha-tubulin from specific regions of the A-tubule. *Journal of cell science* 20(2):405-439.

13.   Schaedel L*, et al.* (2015) Microtubules self-repair in response to mechanical stress. *Nat Mater* 14(11):1156-1163.

14.   Alushin GM*, et al.* (2014) High-resolution microtubule structures reveal the structural transitions in alphabeta-tubulin upon GTP hydrolysis. *Cell* 157(5):1117-1129.

15.   Zhang R, Alushin GM, Brown A, & Nogales E (2015) Mechanistic Origin of Microtubule Dynamic Instability and Its Modulation by EB Proteins. *Cell* 162(4):849-859.

16.   Manka SW & Moores CA (2018) The role of tubulin-tubulin lattice contacts in the mechanism of microtubule dynamic instability. *Nature structural & molecular biology* 25(7):607-615.

470 17. Zhang R, LaFrance B, & Nogales E (2018) Separating the effects of nucleotide and EB
471   binding on microtubule structure. *Proceedings of the National Academy of Sciences of*
472   *the United States of America* 115(27):E6191-E6200.
473 18. Zhang R, Roostalu J, Surrey T, & Nogales E (2017) Structural insight into TPX2-stimulated
474   microtubule assembly. *Elife* 6.
475 19. Manka SW & Moores CA (2018) Microtubule structure by cryo-EM: snapshots of
476   dynamic instability. *Essays Biochem* 62(6):737-751.
477 20. Miki-Noumura T & Kamiya R (1979) Conformational change in the outer doublet
478   microtubules from sea urchin sperm flagella. *The Journal of cell biology* 81(2):355-360.
479 21. Kirima J & Oiwa K (2018) Flagellar-associated Protein FAP85 Is a Microtubule Inner
480   Protein That Stabilizes Microtubules. *Cell Struct Funct* 43(1):1-14.
481 22. Sui H & Downing KH (2010) Structural basis of interprotofilament interaction and lateral
482   deformation of microtubules. *Structure* 18(8):1022-1031.
483 23. Schmidt-Cernohorska M*, et al.* (2019) Flagellar microtubule doublet assembly in vitro
484   reveals a regulatory role of tubulin C-terminal tails. *Science* 363(6424):285-288.
485 24. Witman GB (1986) Isolation of Chlamydomonas flagella and flagellar axonemes.
486   *Methods in enzymology* 134:280-290.
487 25. Zheng SQ*, et al.* (2017) MotionCor2: anisotropic correction of beam-induced motion for
488   improved cryo-electron microscopy. *Nature methods* 14(4):331-332.
489 26. Zivanov J*, et al.* (2018) New tools for automated high-resolution cryo-EM structure
490   determination in RELION-3. *Elife* 7.
491 27. Zhang K (2016) Gctf: Real-time CTF determination and correction. *Journal of structural*
492   *biology* 193(1):1-12.
493 28. Tang G*, et al.* (2007) EMAN2: an extensible image processing suite for electron
494   microscopy. *Journal of structural biology* 157(1):38-46.
495 29. Webb B & Sali A (2014) Protein structure modeling with MODELLER. *Methods Mol Biol*
496   1137:1-15.
497 30. Adams PD*, et al.* (2010) PHENIX: a comprehensive Python-based system for
498   macromolecular structure solution. *Acta Crystallogr D Biol Crystallogr* 66(Pt 2):213-221.
499 31. Pettersen EF*, et al.* (2004) UCSF Chimera--a visualization system for exploratory research
500   and analysis. *J Comput Chem* 25(13):1605-1612.
501 32. Goddard TD*, et al.* (2018) UCSF ChimeraX: Meeting modern challenges in visualization
502   and analysis. *Protein Sci* 27(1):14-25.
503 33. Pazour GJ, Agrin N, Leszyk J, & Witman GB (2005) Proteomic analysis of a eukaryotic
504   cilium. *The Journal of cell biology* 170(1):103-113.
505 34. Oda T, Yanagisawa H, Kamiya R, & Kikkawa M (2014) A molecular ruler determines the
506   repeat length in eukaryotic cilia and flagella. *Science* 346(6211):857-860.
507 35. Kangkang Song ZS, Xiaofeng Fu, Xiaochu Lou, Nikolaus Grigorieff, Daniela Nicastro
508   (2018) Structure of the ciliary axoneme at nanometer resolution reconstructed by
509   TYGRESS. *BioRvix*.
510
511

Fig. 1

Network of the MIPs are woven into the tubulin lattice. Schematic cartoon of the doublet from *Tetrahymena* viewed from the tip of the cilia. PF numbers are shown, and MIPs are colored as the right panel. (B) Surface rendering of the 48-nm repeating unit of the doublet [colors according to (A)]. Scale bar, 10 nm. Views of (C-E) is indicated in (B). (C) The weaving network of MIPs inside the tubulin lattice. Tubulin densities were removed for clarity. (D and E) Insertions of the MIPs woven into the tubulin lattice. Mostly α-helical branches from MIP densities were going into (orange arrowheads) or through (red arrowheads) the tubulin lattice the tubulin lattice. The branch from MIP2 interacts with MIP7 densities and branches from fMIP-A6A7 also reach to the external surface or outer filament-A6A7 as shown by red arrowheads.

1
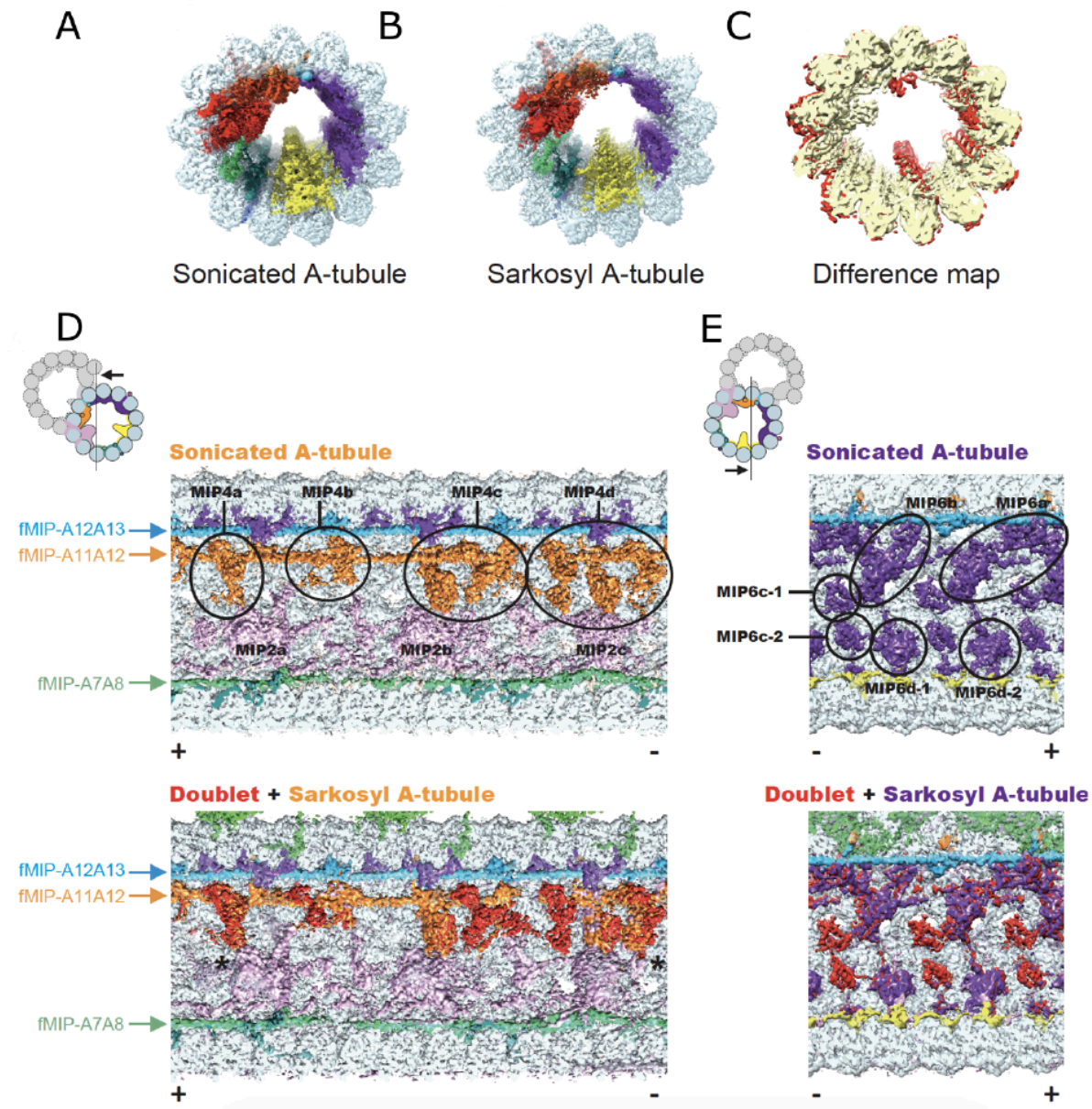
Fig. 2

Fig. 2

Sarkosyl treatment removes some MIPs from the doublet

(A and B) Surface rendering of the sonicated A-tubule (A) and Sarkosyl A-tubule (B) maps. (C) Difference map between the sonicated and Sarkosyl A-tubule maps. Superimposition of the two maps revealed the missing MIP densities in the Sarkosyl A-tubule map (red regions). Parts of MIP2 and MIP6 were missing in Sarkosyl A-tubule map. (C and D) Sonicated A-tubule map (top) and the overlap of doublet and Sarkosyl A-tubule maps (bottom). The MIP4 region or MIP6 region from doublet (red) are mapped onto corresponding regions from Sarkosyl A-tubule map (MIP4 in orange and MIP6 in purple). The views are indicated in the illustrations on the top left. Remaining fMIPs are indicated from the side. The coloring of MIP2 and MIP4 is different from other figures to avoid confusion (see the illustration for the coloring). Some densities at MIP4 and MIP6 regions were missing after the Sarkosyl treatment while the fMIPs appeared intact. The slight shifts in MIP4a at both + and - end sides (indicated by asterisks) are due to lateral compaction of the tubulin lattice. Polarities of microtubules are indicated by + and -.
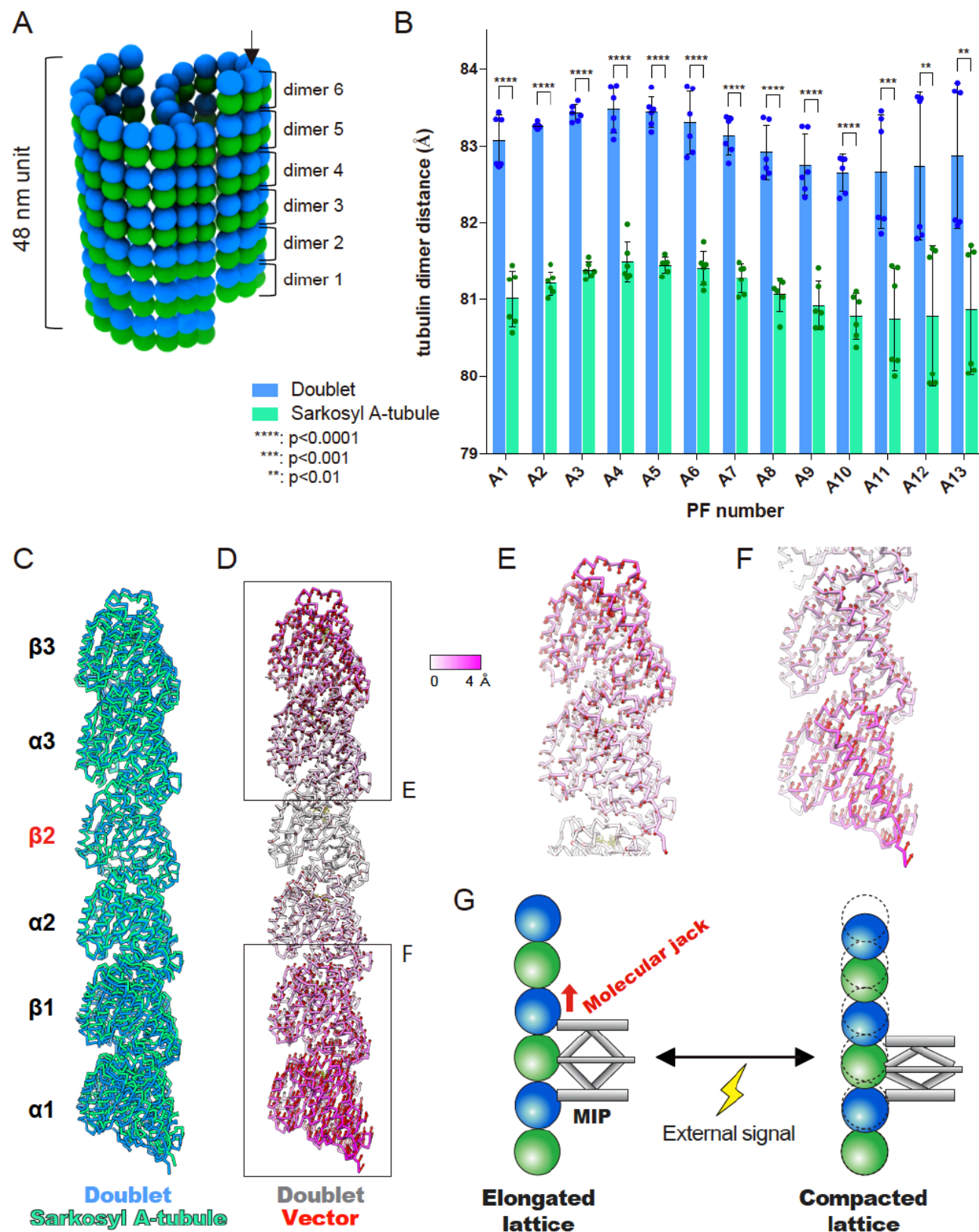
2

Fig. 3

Fig. 3

Longitudinal tubulin lattice length is regulated by MIPs.

Schematics of six tubulin dimers in 48-nm repeating units of the doublet. Dimer distances were measured for each PF as in (Fig. S4A). (B) Plot of tubulin dimer distances from doublet and the Sarkosyl A-tubule. Raw measurement (n=6) and mean value with standard deviation for each PF are shown. The average value of each PF from Sarkosyl A-tubule shows lateral compression of ~2 Å. Some PFs showed a bimodal distribution of dimer distances. Statistical analysis was performed by multiple *t*-tests (see also table S2). (C) Comparison of tubulin models refined in PF-A12 from doublet (blue) and Sarkosyl A-tubule (green) showing a lateral compaction after missing some MIPs. Models were aligned by β2-tubulin. (D) Tubulin model of PF-A12 from doublet colored according to the degree of displacement. Vectors of the Cα displacement toward the Sarkosyl A-tubule model are shown in red. (E and F) Close-up views of the tubulins from the periphery with vectors. (G) Schematic diagram of MIP's function in regulating tubulin lattice length. Some MIPs work as a molecular jack and change tubulin lattice according to the external signals.
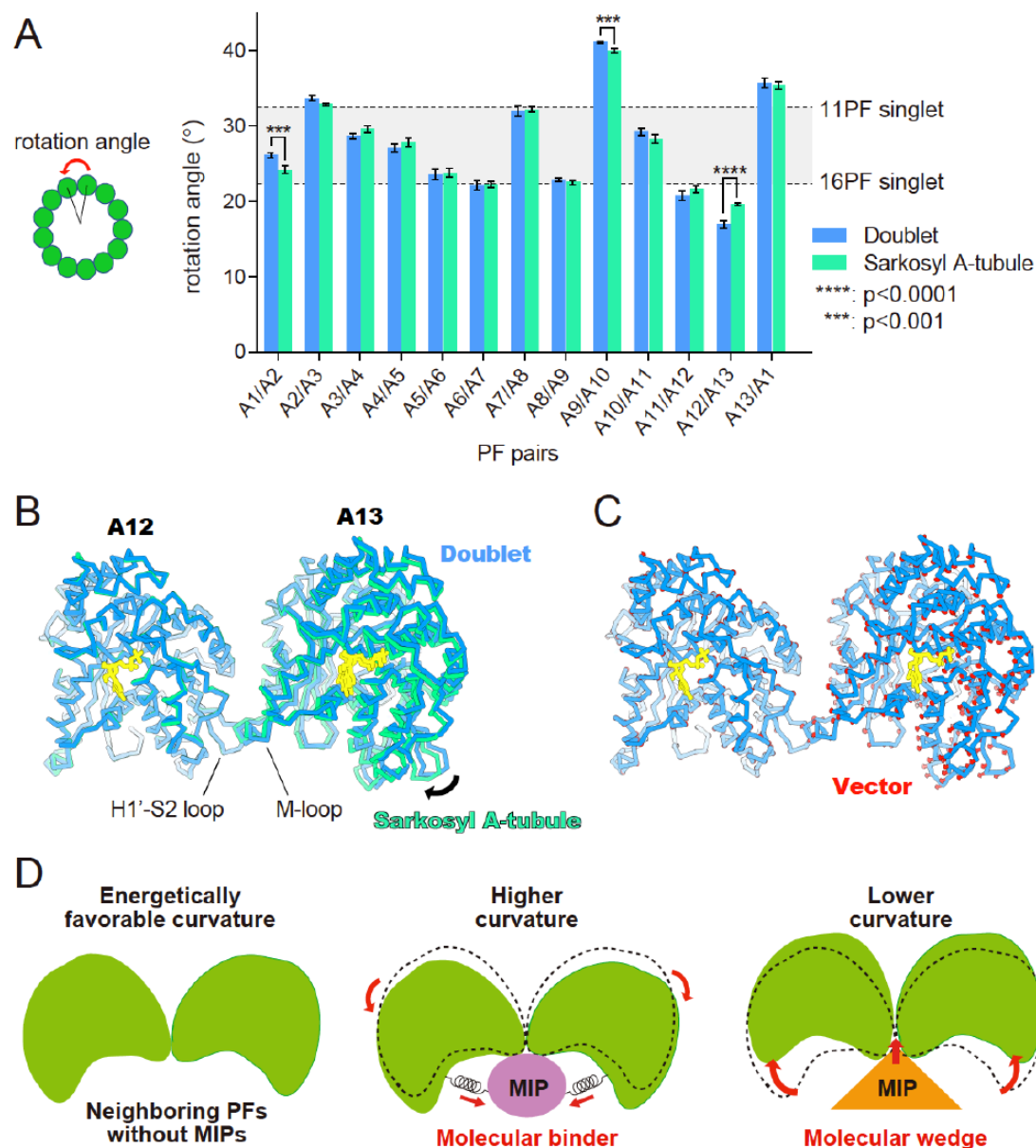
Fig. 4

MIPs fix the tubulin lattice into extreme curvature. Plot of angles between neighboring PFs in the doublet and Sarkosyl A-tubule. Rotation angles were measured as shown in the schematic diagram on the left and mean values were plotted (see also Fig. S5A and Table S3). Error bars represent standard deviation. Multiple *t*-tests were performed to compare the mean values, and PF pairs showing *p*-values smaller than 0.001 are highlighted by asterisks (see also table S4). The gray area in the plot represents the PF pair angles commonly seen for *in vitro* reconstituted singlets (1). (B) Overlap of the models of PF pair-A12/A13 from the doublet (green) and Sarkosyl A-tubule (blue) with the tubulin unit of PF-A12 aligned reveals ~3° difference in rotation (black arrow). (C) The model of PFs-A12/A13 from the doublet with the vectors (red) of the displacement of Cα of each residue compared to the Sarkosyl A-tubule model. Nucleotides: yellow. (D) MIPs regulate the angles between PFs. Without MIPs, tubulin lattice takes energetically favorable curvature as singlets. Some MIPs work as molecular binders which holds adjacent tubulin pairs together so that it will take a higher curvature. Other MIPs work as molecular wedges and opens the PF pairs inducing a lower curvature.

5
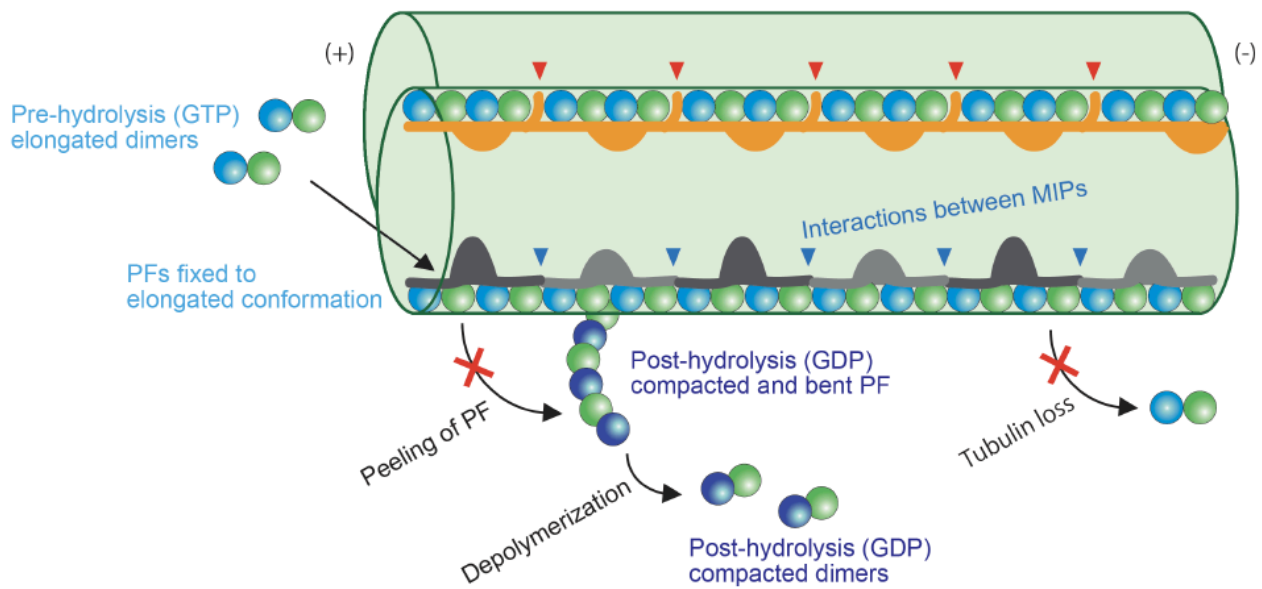
Fig. 5

Fig. 5. Model of stabilization mechanisms of the doublet tubulin lattice by MIPs.
First, elongated tubulin dimers in GTP pre-hydrolysis state are incorporated into the tubulin lattice. This elongated and stable conformation is fixed after assembly into the doublet lattice through the interactions with the MIPs. The network of MIPs (blue arrowheads) also holds the tubulin lattice from the inside to prevent the loss of tubulin molecules or breakage at the middle part. At the plus end, MIPs prevent the peeling of PFs and depolymerization by keeping PFs in a stable and elongated conformation. Hence, double is stabilized by MIPs with several different levels to ensure that it can withstand the mechanical stress and prevent catastrophic events for the cilia. Some MIPs have insertions into tubulin lattice (red arrowheads), causing the larger inter-dimer gap and bimodal dimer distance.

Fig. S1. Related to doublet microtubule structure.

(A) Schematics of fractionation of the axoneme in this study. Doublet microtubule were split from axoneme, and outside proteins were removed to obtain simpler sample for cryo-EM. A-tubules were obtained either sonication or Sarkosyl treatment. (B) SDS-PAGE gel of the fractionated axoneme. From the gel, Sarkosyl-treated fraction was less complex than the doublet fraction consistent with the missing densities in the EM result. (C) A typical cryo-EM image of doublet fraction showing both doublets (red arrowheads) and A-tubules (orange arrowheads) due to sonication process. (D) A representative cryo-EM image of the Sarkosyl-treated fraction showing the A-tubules (orange arrowheads). Scale bars in (C and D), 100 nm. (E) Gold-standard Fourier Shell Correlation of the doublet, sonicated A-tubule and Sarkosyl A-tubule maps. (F) Model of doublet structure with other associated structures. The parts shown by gray and dashed lines were removed in our preparation and not seen in our map. The locations of outer arm dynein-regulator (OA-R) and inner arm dynein-regulator (IA-R) are adopted from (2). (G) Surface rendering of the doublet showing PFs-A9, A10 and B1. α-tubulin is shown in green and β-tubulin in blue. (H) A view of branches from fMIPs reaching outside surface and the outside densities at B-tubule region. (I) A view of doublet map showing the branch of MIP2 (indicated by red arrowhead) going between PF pairs-A10/B1 and reaching outside of the doublet tubulin lattice. The area is the same with Fig. 1D but with a different depth. The views (G-I) are shown in (F). (J) A view of ribbon region of doublet map. fMIPs appeared as single α-helical structures running in between the inner ridges of the PF pairs-A11/A12 and A12/A13. The globular MIPs and fMIPs are connected by α-helical branches. (K) A view showing outside filament-A6A7. Red arrowheads indicate the interactions between fMIP-A6A7 and outside filament. Outside filament-A6A7 appeared as 24-nm repeating unit. (L and M) Views showing branches from fMIPs-A11A12 and A12A13. Previously, we proposed that fMIP-A12A13 has branches which pokes into the tubulin lattice every 16-nm unit (3). With higher resolution, these branches (red arrowheads) were found to be derived from both fMIPs-A11A12 and A12A13.
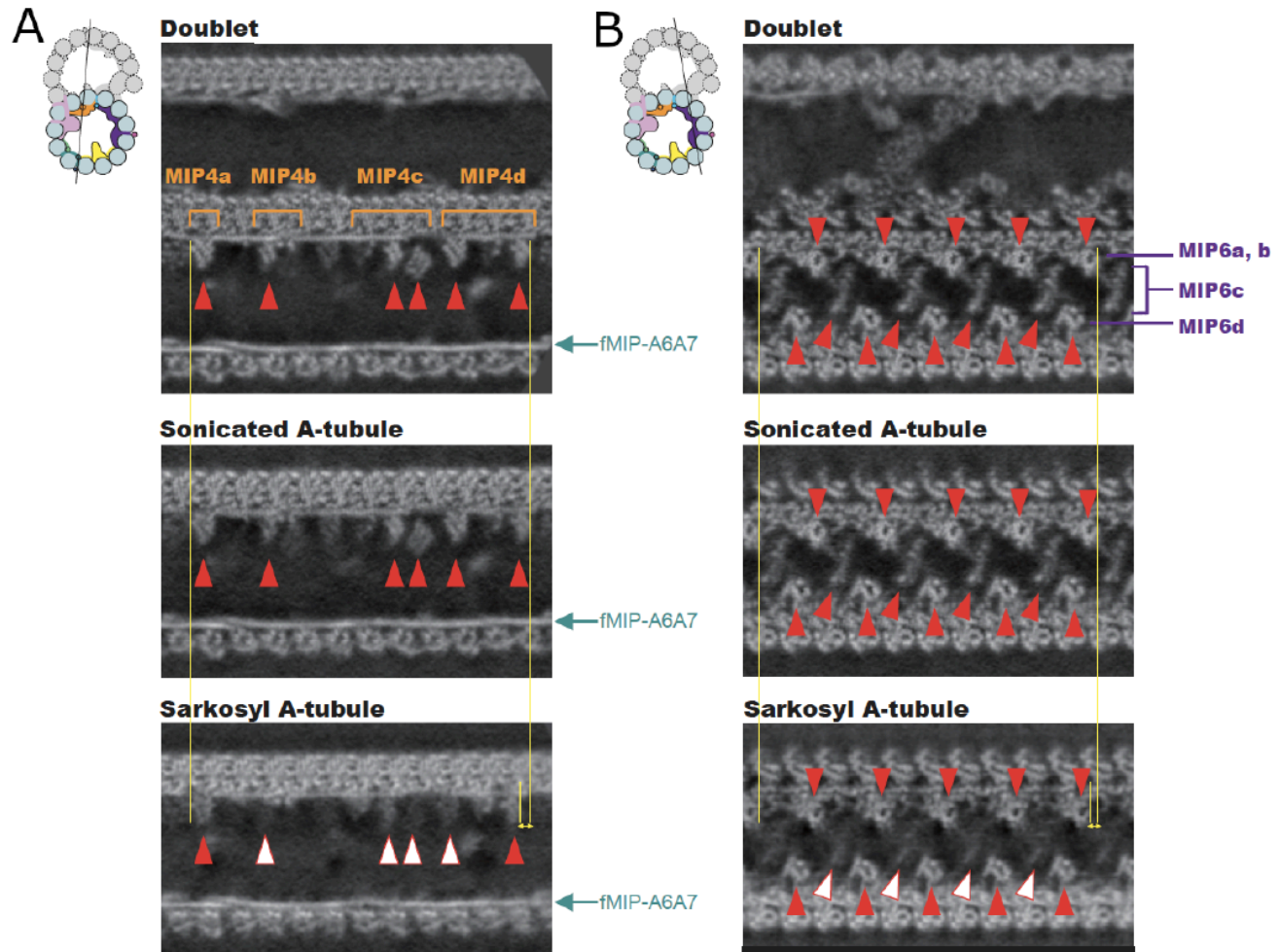
8

Fig. S2

Fig. S2. Comparison of MIPs from the doublet, sonicated A-tubule and Sarkosyl A-tubule maps.
(A and B) Slices through the maps of the doublet, sonicated A-tubule and Sarkosyl A-tubule. Black lines in illustrations indicate the locations of the slices. MIP4 and MIP6 were preserved in sonicated A-tubule structure as shown by red arrowheads. Missing parts of these MIPs in Sarkosyl A-tubule map are indicated by empty arrowheads. fMIP-A6A7 densities are shown by arrows in (A). Yellow lines and double-headed arrows indicate the shifts of the MIPs in the longitudinal direction due to compaction of the tubulin lattice in Sarkosyl A-tubule.
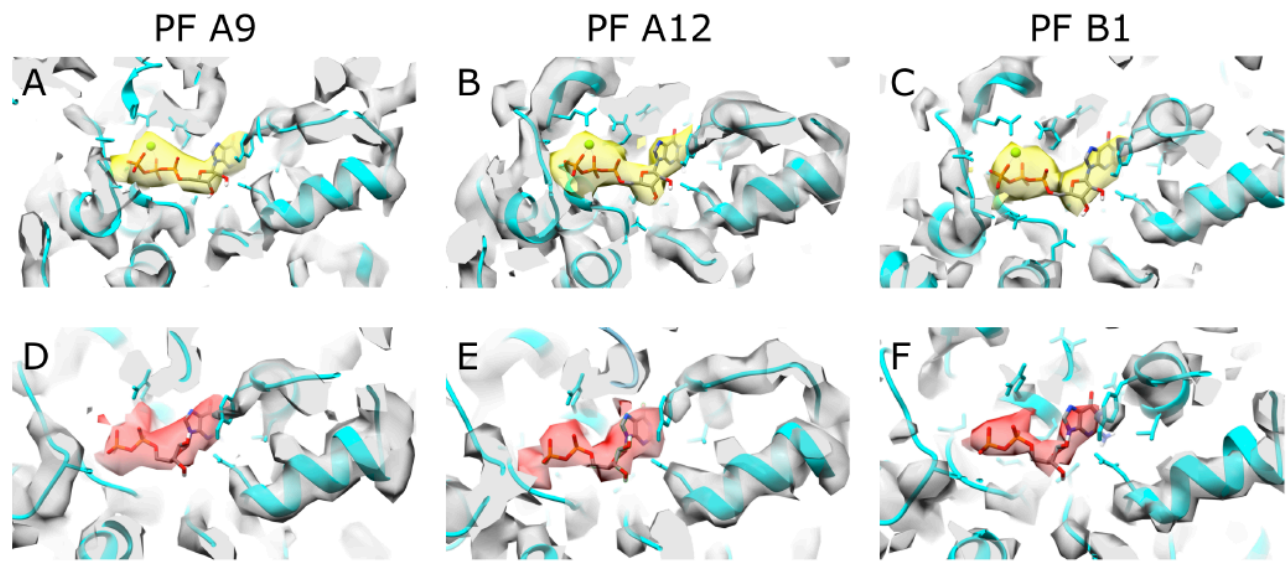
Fig. S3

Fig. S3. Nucleotide states in the doublet

Densities corresponding to GTP are observed in α-tubulins of PF A9 (A), A12 (B) and B1 (C) while densities corresponding to GDP are observed in β-tubulins of PF A9 (D), A12 (E) and B1 (F).

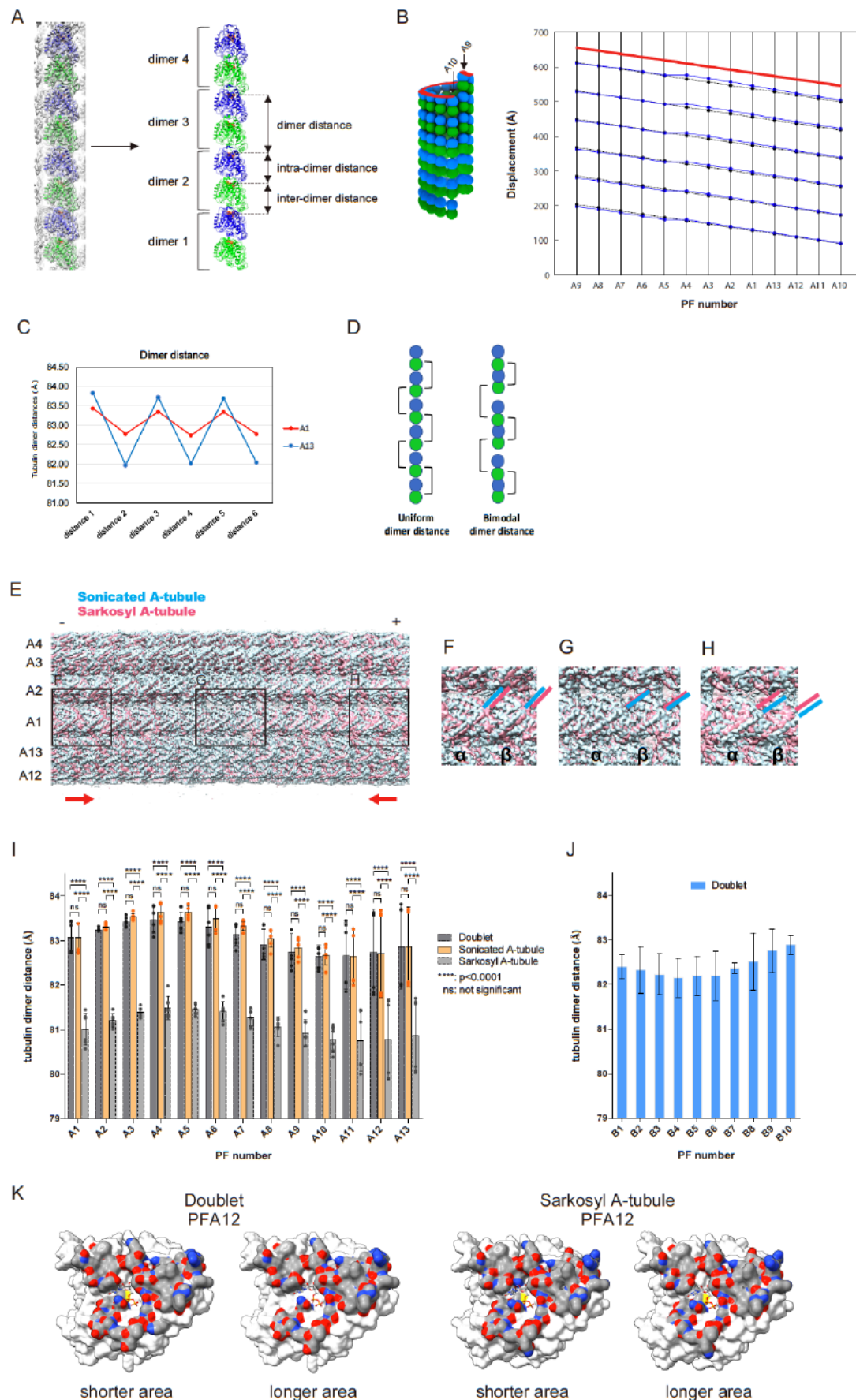Fig. S4

Fig. S4. Data related to longitudinal tubulin dimer distance.

(A) Details of measurement of the tubulin dimer distances. First, tubulin monomer models were fitted to each PF (left panel) and intra- and inter-dimer distances were measured as distances between nucleotide molecules (right panel). Dimer distances were obtained as sums of intra- and inter-dimer distances. Nucleotides are shown in orange. (B) Plot of the tubulin dimer distances of the A-tubule from the doublet (blue) and 13-PF singlet (1) (black). Tubulin lattice is cut and opened at the seam as in the schematic diagram. Despite having a 13-3 B-lattice as a 13-PF singlet, the A-tubule from doublet showed non-uniform tubulin dimer distances and Z-shifts. (C) Oscillation of tubulin dimer distances. The dimer distances from PFs-A1 and A13 of the doublet, where bimodal distributions were seen, were plotted in the same order as in 48-nm unit. The dimer distances oscillated with every two tubulin units (~16 nm), which coincides with repeating unit of MIPs at these regions. (D) Models of tubulin lattice with uniform dimer distance and bimodal dimer distance. In case that tubulin molecules are having same inter-dimer distances, the tubulin dimer distance will be uniform as in left panel. If tubulin molecules have alternate shorter and longer inter-dimer gaps, the tubulin dimer distance will be bimodal and oscillatory as in right panel. The distance is exaggerated for clarity and not to scale. (E-H) Comparison of the density maps of sonicated and Sarkosyl A-tubules. In the middle part, tubulin fitted well as in (G). On the other hand, as it gets closer to both ends, tubulin densities from Sarkosyl A-tubule map appeared shifted toward the middle (F and H), which means that Sarkosyl A-tubule tubulin lattice is shorter than that of sonicated A-tubule. Red arrows indicate the tubulin shift directions from both + and - ends. Locations of H12 of tubulin are indicated by pink or blue lines. (I) Plot of tubulin dimer distances from sonicated A-tubule map. Values of A-tubule from doublet map and Sarkosyl A-tubule map from Fig. 2B are shown in gray for comparison. For statistical analysis, two-way ANOVA followed by Turkey's multiple comparison test was performed. For all PFs, changes between doublet and sonicated A-tubule were not significant ($p > 0.01$). Sonicated A-tubule also shows a bimodal distribution. (J) Plot of tubulin dimer distances of B-tubule part from the doublet. Lattice length of the B-tubule was generally shorter than the A-tubule from doublet (see also table S5). (K) Comparison of interfaces of the β-tubulin at the dimer interface. The interacting residues were colored. The interface of the shorter distance pairs at PF-A12 from doublet showed more residues involved in interactions compared with that of the longer distance pairs (1,681 vs. 1,250 A^2). There was even more interacting interface in the shorter distance area at PF-A12 from Sarkosyl A-tubule compared with the longer distance area (1,850 vs. 1,521 Å^2).
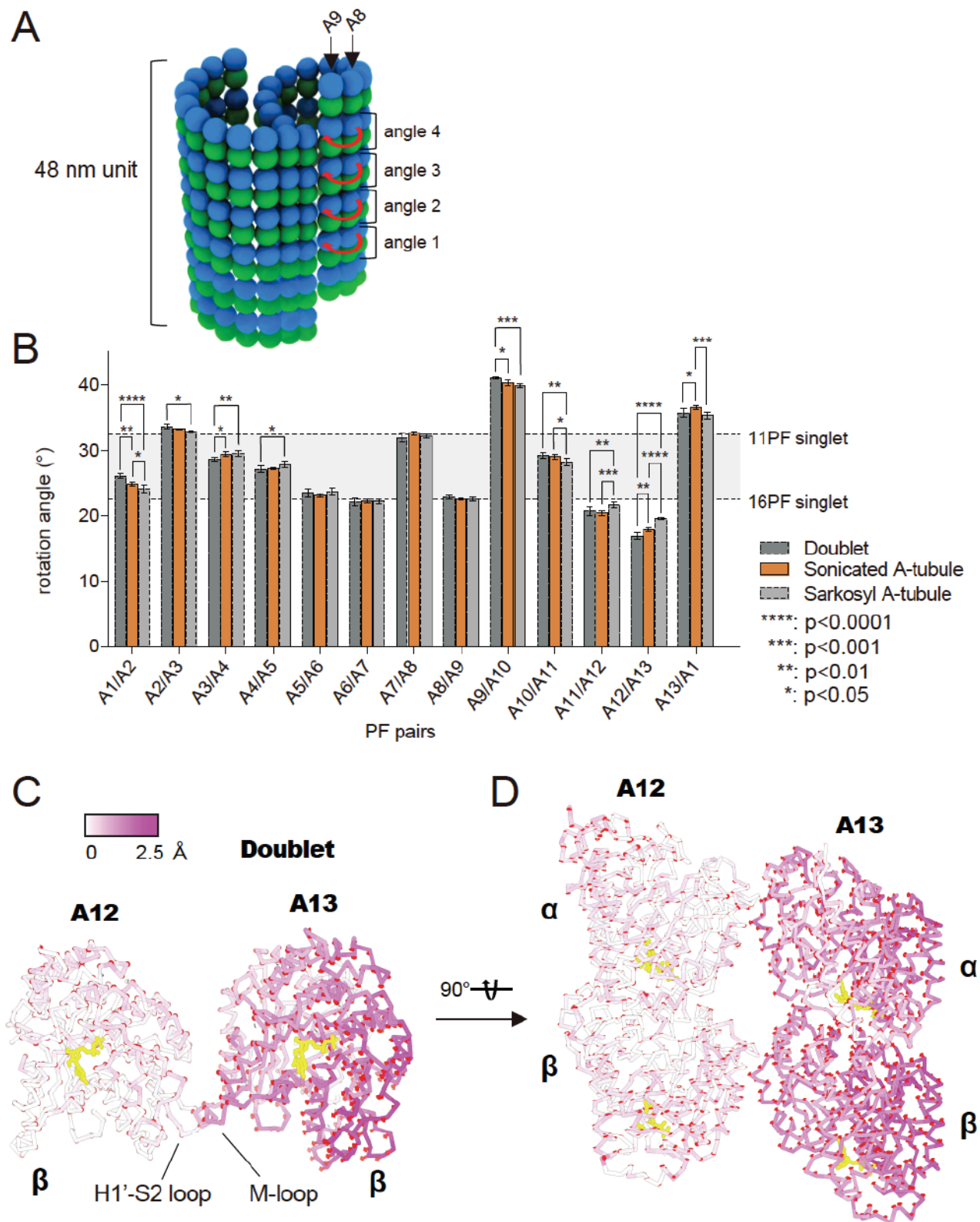
Fig. S5

Fig. S5. Data related to PF angle change.

(A) Schematics of measurement of PF angles. Angles were measured using four tubulin pairs from each PF pair in the 48-nm unit as indicated by red arrows. PF pair-A8/A9 is shown as an example here. (B) Plots of PF angles from sonicated A-tubule map. Values of doublet and Sarkosyl A-tubule from Fig. 2A are shown in gray for comparison. Two-way ANOVA followed by Turkey's multiple comparison test was performed for statistical analysis here. Curvatures of PFs A5-A9 where MIPs were preserved (Fig. 1, F to H) were the least affected. (C and D) Comparison of PF pair-A12/A13 models from doublet and Sarkosyl A-tubule. View in (C) is the same as Fig. 3B. The models are aligned on the tubulin dimer in PF-A12. The display model is from the PF pair-A12/A13 from the doublet and colored based on the displacement of Cα. The displacement vectors from the doublet to the Sarkosyl A-tubule are shown in red. The displacement vectors clearly show the rotation of the tubulin dimer in A13 in the Sarkosyl A-tubule. Yellow, nucleotides.

Table S1. Tubulin dimer distances of the A-tubule lattice.

	Dimer distances (intra- / inter-dimer distances) from doublet (Å) (mean ± SD, n = 6)	Dimer distances (intra- / inter-dimer distances) from sonicated A-tubule (Å) (mean ± SD, n = 6)	Dimer distances (intra- / inter-dimer distances) from Sarkosyl A-tubule (Å) (mean ± SD, n = 6)
A1	83.1 ± 0.309 (41.8 ± 0.0352 / 41.3 ± 0.299)	83.1 ± 0.313 (41.8 ± 0.222 / 41.3 ± 0.300)	81.0 ± 0.333 (41.1 ± 0.106 / 39.9 ± 0.253)
A2	83.3 ± 0.0354 (41.7 ± 0.0507 / 41.5 ± 0.0636)	83.3 ± 0.0672 (41.8 ± 0.0474 / 41.6 ± 0.0796)	81.2 ± 0.143 (41.0 ± 0.0868 / 40.2 ± 0.0929)
A3	83.4 ± 0.0988 (41.8 ± 0.0242 / 41.6 ± 0.0975)	83.5 ± 0.0696 (41.8 ± 0.0351 / 41.7 ± 0.0549)	81.4 ± 0.0965 (40.8 ± 0.0455 / 40.6 ± 0.0965)
A4	83.5 ± 0.274 (41.8 ± 0.0460 / 41.6 ± 0.255)	83.6 ± 0.195 (41.8 ± 0.0457 / 41.8 ± 0.191)	81.5 ± 0.242 (40.8 ± 0.0511 / 40.7 ± 0.215)
A5	83.4 ± 0.184 (41.9 ± 0.0414 / 41.6 ± 0.199)	83.6 ± 0.127 (41.9 ± 0.0344 / 41.8 ± 0.154)	81.4 ± 0.0944 (40.7 ± 0.118 / 40.7 ± 0.198)
A6	83.3 ± 0.369 (41.8 ± 0.0730 / 41.5 ± 0.345)	83.5 ± 0.271 (41.8 ± 0.0586 / 41.7 ± 0.224)	81.4 ± 0.206 (41.0 ± 0.112 / 40.4 ± 0.216)
A7	83.1 ± 0.228 (41.7 ± 0.0762 / 41.4 ± 0.192)	83.3 ± 0.0896 (41.8 ± 0.558 / 41.5 ± 0.102)	81.3 ± 0.175 (41.0 ± 0.0914 / 40.3 ± 0.109)
A8	82.9 ± 0.319 (41.7 ± 0.0786 / 41.2 ± 0.253)	83.0 ± 0.182 (41.7 ± 0.0337 / 41.3 ± 0.173)	81.1 ± 0.204 (40.8 ± 0.0403 / 40.2 ± 0.207)
A9	82.8 ± 0.367 (41.7 ± 0.0653 / 41.0 ± 0.337)	82.8 ± 0.198 (41.7 ± 0.0650 / 41.1 ± 0.239)	80.9 ± 0.285 (40.9 ± 0.138 / 40.1 ± 0.295)
A10	82.7 ± 0.221 (41.6 ± 0.0545 / 41.0 ± 0.218)	82.7 ± 0.202 (41.7 ± 0.0753 / 41.0 ± 0.226)	80.8 ± 0.268 (40.7 ± 0.104 / 40.1 ± 0.261)
A11	82.7 ± 0.676 (41.7 ± 0.0840 / 41.0 ± 0.649)	82.6 ± 0.575 (41.7 ± 0.0583 / 41.0 ± 0.593)	80.7 ± 0.610 (40.7 ± 0.0681 / 40.0 ± 0.590)
A12	82.7 ± 0.875 (41.6 ± 0.0900 / 41.1 ± 0.960)	82.7 ± 0.912 (41.7 ± 0.0462 / 41.0 ± 0.938)	80.8 ± 0.836 (40.7 ± 0.0542 / 40.1 ± 0.865)
A13	82.9 ± 0.870 (41.7 ± 0.0443 / 41.2 ± 0.908)	82.9 ± 0.820 (41.7 ± 0.0304 / 41.1 ± 0.836)	80.9 ± 0.772 (40.7 ± 0.0775 / 40.1 ± 0.833)
All*	83.1 ± 0.540 (41.7 ± 0.0937 / 41.3 ± 0.516)	83.1 ± 0.546 (41.8 ± 0.0810 / 41.4 ± 0.516)	81.1 ± 0.485 (40.8 ± 0.158 / 40.3 ± 0.483)

*For all PF results, mean values with SD calculated from all PFs (n = 78) are shown

Table S2. *p*-values from multiple *t*-tests of tubulin dimer distances.

	p-values doublet vs sonicated A-tubule	*p*-values doublet vs Sarkosyl A-tubule	*p*-values sonicated A-tubule vs Sarkosyl A-tubule
A1/A2	0.977	0.00000144	0.00000147
A2/A3	0.129	0.0000000000289	0.0000000000441
A3/A4	0.0729	0.0000000000155	0.00000000000212
A4/A5	0.266	0.000000272	0.0000000252
A5/A6	0.0723	0.00000000105	0.0000000000283
A6/A7	0.380	0.00000151	0.0000000818
A7/A8	0.110	0.0000000495	0.000000000478
A8/A9	0.447	0.000000692	0.0000000164
A9/A10	0.651	0.00000492	0.000000216
A10/A11	0.857	0.000000284	0.000000183
A11/A12	0.966	0.000842	0.000491
A12/A13	0.966	0.00483	0.00594
A13/A1	0.983	0.00319	0.00270

Table S3. Angles between PFs.

	Doublet (°) (mean ± SD, n = 4)	Sonicated A-tubule (°) (mean ± SD, n = 4)	Sarkosyl A-tubule (°) (mean ± SD, n = 4)
A1/A2	26.1 ± 0.341	24.9 ± 0.231	24.2 ± 0.448
A2/A3	33.7 ± 0.303	33.3 ± 0.0913	32.9 ± 0.159
A3/A4	28.7 ± 0.273	29.4 ± 0.295	29.6 ± 0.410
A4/A5	27.1 ± 0.426	27.2 ± 0.125	27.8 ± 0.458
A5/A6	23.6 ± 0.571	23.2 ± 0.211	23.8 ± 0.505
A6/A7	22.2 ± 0.542	22.3 ± 0.245	22.2 ± 0.358
A7/A8	32.0 ± 0.596	32.6 ± 0.261	32.2 ± 0.304
A8/A9	22.9 ± 0.229	22.6 ± 0.115	22.5 ± 0.254
A9/A10	41.1 ± 0.122	40.3 ± 0.351	40.0 ± 0.243
A10/A11	29.2 ± 0.367	29.1 ± 0.336	28.3 ± 0.523
A11/A12	20.8 ± 0.577	20.5 ± 0.291	21.7 ± 0.393
A12/A13	16.9 ± 0.480	17.9 ± 0.241	19.6 ± 0.115
A13/A1	35.8 ± 0.542	36.5 ± 0.286	35.4 ± 0.414

17

Table S4. *p*-values from multiple *t*-tests of PF-pair angles.

	p-values doublet vs sonicated A-tubule	*p*-values doublet vs Sarkosyl A-tubule	*p*-values sonicated A-tubule vs Sarkosyl A-tubule
A1/A2	0.00214	0.000941	0.0448
A2/A3	0.0727	0.00820	0.0130
A3/A4	0.0162	0.0188	0.647
A4/A5	0.711	0.0917	0.0629
A5/A6	0.314	0.631	0.102
A6/A7	0.633	0.865	0.687
A7/A8	0.122	0.569	0.103
A8/A9	0.0758	0.145	0.935
A9/A10	0.0102	0.000299	0.174
A10/A11	0.605	0.0407	0.0669
A11/A12	0.470	0.0708	0.00599
A12/A13	0.0225	0.0000857	0.0000313
A13/A1	0.0697	0.371	0.00717

Table S5. Tubulin dimer distances of the B-tubule from doublet.

	Dimer distances from doublet B-tubule (Å) (mean ± SD, n = 6)
B1	82.4 ± 0.258
B2	82.3 ± 0.476
B3	82.2 ± 0.422
B4	82.2 ± 0.395
B5	82.2 ± 0.401
B6	82.2 ± 0.502
B7	82.4 ± 0.111
B8	82.5 ± 0.581
B9	82.8 ± 0.443
B10	82.9 ± 0.195
All*	82.4 ± 0.468

*For all PF results, mean values with SD calculated from all PFs (n = 60) are shown